LETTER

Stable amorphous georgeite as a precursor to a high–activity catalyst

Simon A. Kondrat[1], Paul J. Smith[1], Peter P. Wells[2,3], Philip A. Chater[4,5], James H. Carter[1], David J. Morgan[1], Elisabetta M. Fiordaliso[6], Jakob B. Wagner[6], Thomas E. Davies[1,5], Li Lu[7], Jonathan K. Bartley[1], Stuart H. Taylor[1], Michael S. Spencer[1], Christopher J. Kiely[7], Gordon J. Kelly[8], Colin W. Park[8], Matthew J. Rosseinsky[5] & Graham J. Hutchings[1]

Copper and zinc form an important group of hydroxycarbonate minerals that include zincian malachite, aurichalcite, rosasite and the exceptionally rare and unstable—and hence little known and largely ignored[1]—georgeite. The first three of these minerals are widely used as catalyst precursors[2–4] for the industrially important methanol-synthesis and low-temperature water–gas shift (LTS) reactions[5–7], with the choice of precursor phase strongly influencing the activity of the final catalyst. The preferred phase[2,3,8–10] is usually zincian malachite. This is prepared by a co-precipitation method that involves the transient formation of georgeite[11]; with few exceptions[12] it uses sodium carbonate as the carbonate source, but this also introduces sodium ions—a potential catalyst poison. Here we show that supercritical antisolvent (SAS) precipitation using carbon dioxide (refs 13, 14), a process that exploits the high diffusion rates and solvation power of supercritical carbon dioxide to rapidly expand and supersaturate solutions, can be used to prepare copper/ zinc hydroxycarbonate precursors with low sodium content. These include stable georgeite, which we find to be a precursor to highly active methanol-synthesis and superior LTS catalysts. Our findings highlight the value of advanced synthesis methods in accessing unusual mineral phases, and show that there is room for exploring improvements to established industrial catalysts.

For the SAS precipitation process, we initially used copper(II) acetate solutions (Extended Data Fig. 1) with ethanol as the solvent; the result was amorphous copper(II) acetate, which we characterized by X-ray diffraction (XRD) and Fourier transform-infrared (FT-IR) spectroscopy. Adding 5 vol% water as a co-solvent produced a blue precipitate with an IR spectrum exhibiting a broad OH band at $3{,}408\,cm^{-1}$ and CO_3^{2-} bands at 1,470, 1,404 and $829\,cm^{-1}$, which are inconsistent with malachite but closely match the spectrum identifying the rare georgeite phase[1]. Helium pycnometry gave a density of $3.1\,g\,cm^{-3}$ for the SAS-prepared phase; as with mineralogical georgeite, the SAS-prepared phase was amorphous by XRD. We further studied the precipitate by inductively coupled plasma mass spectrometry (ICP-MS) and carbon–hydrogen–nitrogen (CHN) analysis (Extended Data Fig. 2), which gave an ideal formula for the precipitate of $Cu_7(CO_3)_5(OH)_4 \cdot 5H_2O$. We regard this to be a close match to the $Cu_5(CO_3)_3(OH)_4 \cdot 6H_2O$ formula reported for georgeite[1], taking into account that slight variations in composition are anticipated for an amorphous phase[15]. The SAS-prepared and mineralogical forms of georgeite both have a higher CO_3^{2-}/Cu^{2+} molar ratio than malachite (the CO_3^{2-}/Cu^{2+} values being 0.7, 0.6 and 0.5, respectively); this contrasts with previous assertions that georgeite and malachite $(Cu_2CO_3(OH)_2)$ are iso-compositional[16] because georgeite rapidly transformed into malachite. We did not observe such instability for SAS-prepared georgeite, as the rapid solvent extraction produced

georgeite that is effectively dry from the point of precipitation and thus has limited contact with water (which facilitates ageing and transformation to malachite).

When we used mixed copper and zinc acetate solutions (with a 2/1 or 1/1 copper/zinc ratio) for the SAS precipitation, zincian georgeite (with a 2/1 or 1/1 copper/zinc ratio, as judged by ICP-MS) formed with a density, IR spectrum and XRD pattern nearly identical to those of copper-only georgeite (Extended Data Figs 1 and 2); no additional phases—such as smithsonite $(ZnCO_3)$—were discernible by XRD. Scanning transmission electron microscopy (STEM) analysis of zincian georgeite revealed predominantly amorphous material, although a small fraction ($<10\,vol\%$) of CuO_x crystallites with diameters less than 2 nanometres were observed (Extended Data Fig. 3; analysis of georgeite itself was not possible because of its instability under vacuum). In addition, the SAS-derived zincian georgeite had few impurities (such as sodium ions; Extended Data Fig. 2).

We therefore found that it was possible to synthesize stable zincian georgeite by SAS in sufficient quantities to evaluate the catalytic performance of copper/zinc oxide, derived from zincian georgeite, in the methanol-synthesis and LTS reactions. As a control, we synthesized a zincian-malachite precursor—considered the optimal precursor for model copper/zinc-oxide catalysts[3]—by co-precipitation (see Methods). The catalysts used here were not stabilized with alumina, an important promoter and stabilizer of the commercial catalyst[17,18]. Before use, the precursors were subjected to calcination to remove the carbonate, followed by *in situ* reduction to form the active catalyst. The optimal calcination temperature was determined using thermal gravimetric analysis (TGA) with evolved gas analysis (EGA), which showed SAS-prepared georgeite to exhibit three distinct mass losses, and malachite to exhibit a single mass loss, associated with concurrent removal of water and carbon dioxide (Fig. 1). The multistep decomposition of georgeite and zincian georgeite (the 1/1 copper/zinc sample shown in Extended Data Fig. 2) can be separated into three regions: water loss at 80–100 °C, water and carbon dioxide loss at 190–210 °C, and carbon dioxide loss at 315–420 °C (carbonate decomposition). On the basis of this analysis, the precursors were calcined at 300 °C in air for 6 hours: this is below the temperature associated with the evolution of carbon dioxide, and residual carbonate species have been shown to improve the activity of methanol-synthesis catalysts[19]. The calcined material was then reduced *in situ* in dilute hydrogen at 225 °C.

Figure 2 contrasts the activity of our model catalysts with that of commercial catalysts, showing that the catalyst derived from SAS-prepared zincian georgeite is more active than both the catalyst formed from zincian malachite and the standard commercial catalyst. In the case of methanol synthesis, for which our model catalysts showed markedly higher initial productivity (normalized for copper surface area;

[1]Cardiff Catalysis Institute, School of Chemistry, Cardiff University, Main Building, Park Place, Cardiff CF10 3AT, UK. [2]The UK Catalysis Hub, Research Complex at Harwell, Harwell, Oxon OX11 0FA, UK. [3]Kathleen Lonsdale Building, Department of Chemistry, University College London, Gordon Street, London WC1H 0AJ, UK. [4]Diamond Light Source, Didcot OX11 0DE, UK. [5]Department of Chemistry, University of Liverpool, Crown Street, Liverpool L69 7ZD, UK. [6]Center for Electron Nanoscopy, Technical University of Denmark, Fysikvej 307, DK-2800 Kgs Lyngby, Denmark. [7]Department of Materials Science and Engineering, Lehigh University, 5 East Packer Avenue, Bethlehem, Pennsylvania 18015, USA. [8]Johnson Matthey, PO Box 1, Belasis Avenue, Cleveland TS23 1LB, UK.
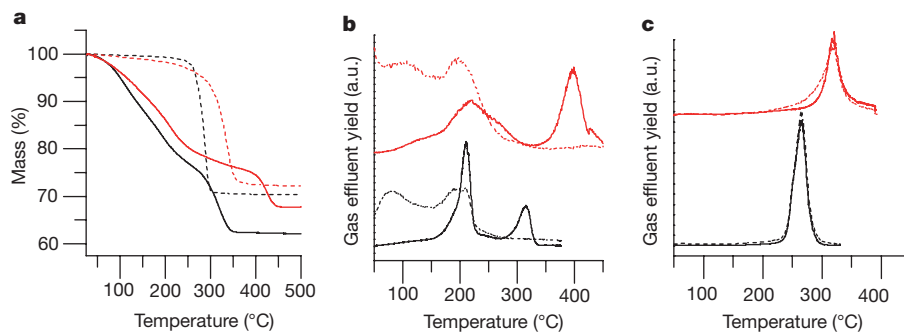
Figure 1 | Thermal gravimetric analysis (TGA) with evolved gas analysis (EGA) of georgeite and malachite. a, TGA of georgeite (black solid line), zincian georgeite (red solid line), malachite (black dotted line) and zincian malachite (red dotted line). **b**, EGA of georgeite (black lines) and zincian georgeite (red lines). **c**, EGA of malachite (black lines) and zincian malachite (red lines). In **b** and **c**, the solid lines indicate CO_2 (fragment with mass 44) and dashed lines indicate H_2O (fragment with mass 18).

Extended Data Fig. 4), the enhancement of activity was short-lived. But in the LTS reaction, the SAS-prepared zincian-georgeite-derived catalyst was far more active and stable over the entire test period; indeed, enhanced activity was apparent at all contact times investigated (Fig. 2). These observations demonstrate that the availability of stable zincian georgeite as a precursor gives access to highly active copper/zinc-oxide catalysts, with the LTS activity and stability maintained

using 30% less copper than is present in a catalyst derived from a 2/1 copper/zinc georgeite (Extended Data Fig. 4).

The stability and quantities of georgeite that are available through SAS allowed us to explore structural origins for its enhanced activity. X-ray-absorption near-edge structure (XANES) data for copper-only georgeite and malachite precursors (Fig. 3a) indicate that both materials contain Cu^{2+} in a distorted octahedral environment[20], in agreement
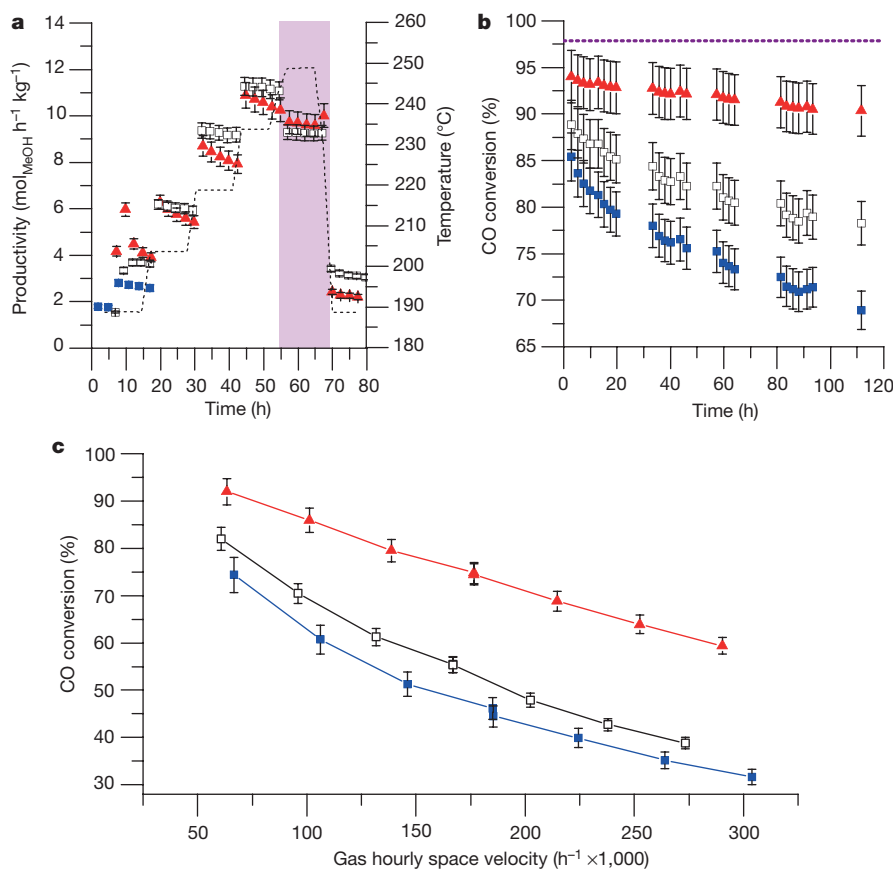
Figure 2 | Comparison of our model catalysts to commercial catalysts. a, Methanol synthesis (shown as mass-normalized, time-on-line methanol production). The dashed line denotes the representative reactor-bed temperature for methanol synthesis. Reaction conditions for methanol synthesis: 190–250 °C (shaded area shows reaction under equilibrium conditions at 250 °C), 25 bar, gas composition $CO/CO_2/H_2/N_2 = 6/9.2/67/17.8$, mass hourly space velocity (MHSV) = 7,200 $kg^{-1} h^{-1}$. The selectivities of all of the catalysts to methanol are greater than 99.96%. **b**, Low-temperature water–gas shift (LTS) reaction (shown as time-on-line CO conversion). The dashed line represents the maximum equilibrium conversion. Reaction conditions for LTS: 220 °C, 27.5 bar, gas composition $H_2O/CO/CO_2/H_2/N_2 = 50/2/8/27.5/12.5$, MHSV = 75,000 $kg^{-1} h^{-1}$. **c**, LTS conversions at different gas hourly space velocities. (Extended Data Fig. 4 shows LTS mass-normalized data, copper mass-normalized productivities/activities, initial copper surface area normalized productivities/activities and product impurities.) Red triangles, zincian-georgeite-derived catalyst; blue squares, co-precipitated zincian-malachite-derived catalyst; open squares, industrial standards (composition of the industrial methanol-synthesis catalyst by wt% is $CuO/ZnO/Al_2O_3 = 60/30/10$; composition of the industrial LTS catalyst by wt% is $CuO/ZnO/Al_2O_3 = 50/33/17$). Error-bar calculations are discussed in Methods.
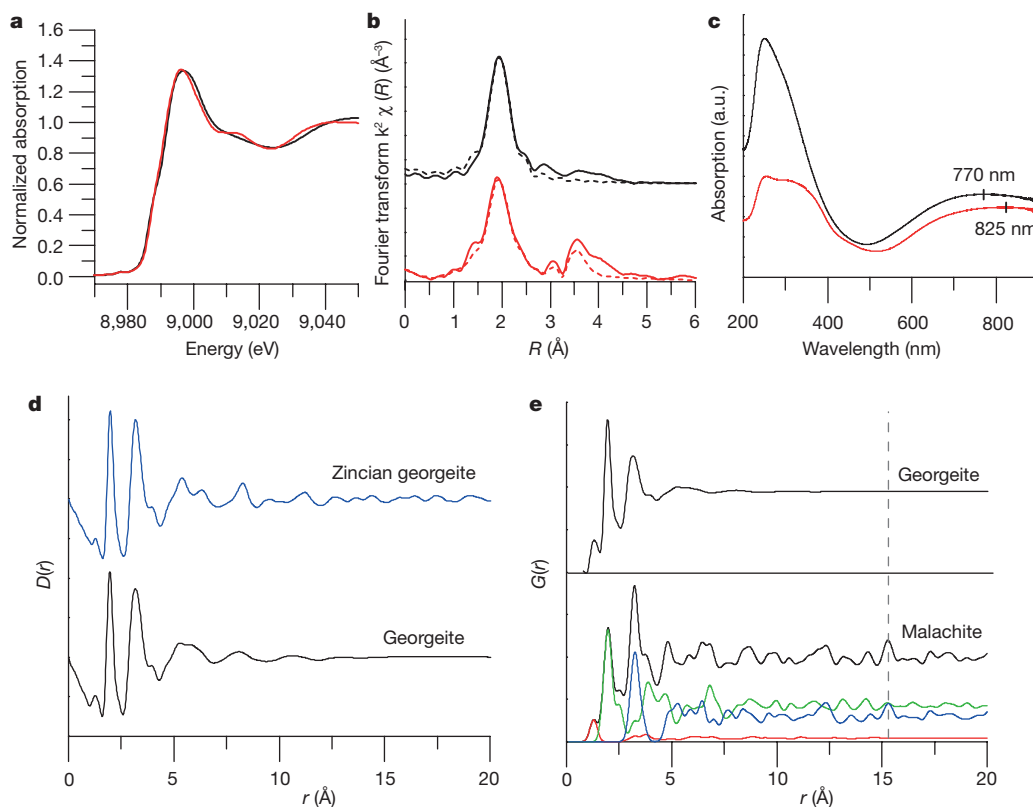
Figure 3 | X-ray absorption fine-edge spectroscopy (XAFS) and X-ray pair distribution function (PDF) analysis. a, Copper K-edge XAFS information on local structure, for malachite (red line) and georgeite (black line). **b**, Fourier transform (FT) of extended X-ray absorption fine-edge spectra (EXAFS) k^2 weighted χ data (Fourier transform k^2 $\chi(R)$), with associated fitting parameters for malachite (red line) and georgeite (black line). Variation in the magnitude of the FT is plotted with distance R (Å) from the Cu absorber; k denotes the fitting window from the χ data. The fit (shown with dashed lines) was modelled on four shorter Cu–O bond distances and two longer Jahn–Teller distorted Cu–O bond distances (Extended Data Table 1). **c**, Ultraviolet–visible spectra for malachite (red line) and georgeite (black line), with centres of d–d

transition bands (based on peak maxima) marked as small vertical lines (zincian phases are shown in Extended Data Fig. 5a). **d**, X-ray PDF data for georgeite and zincian georgeite. $D(r)$ is the probability of finding a pair of atoms, weighted by the scattering power of the pair, at a given distance, r. The probability is scaled to r to emphasize order at greater distances. **e**, Top, observed PDF $G(r)$ data ($G(r)$ is equivalent to $D(r)$, only without scaling by r) for georgeite. Bottom, calculated PDF $G(r)$ data for all of the atom pairs of malachite (black), together with the partial contributions from the most strongly contributing atom pairs: C–O (red), Cu–O (green) and Cu–Cu (blue). The dotted line represents a contribution from crystallographically equivalent Cu atoms in malachite (see text).

with diffuse reflectance ultraviolet–visible spectroscopy (DRS) and extended X-ray absorption fine structure (EXAFS) data (Fig. 3b and Extended Data Table 1). But our analysis also suggests subtle differences in coordination geometries. Specifically, DRS locates the optical band associated with the metal centre(s) in georgeite at 770 nm, whereas the combined bands from the two crystallographic copper centres in malachite occur at 825 nm (ref. 21). Although XANES data for georgeite and malachite are similar, the Fourier transform of the EXAFS χ data (Fig. 3b) shows that malachite has contributions further out from the copper absorber that are correlated to the scattering effects of copper–copper neighbours, whereas there are very few features in the georgeite EXAFS data beyond 2 Å and no evidence of metal–metal correlation. The addition of zinc did not affect metal geometry in georgeite, with no discernible changes appearing in the copper EXAFS data or zinc K-edge XANES or EXAFS χ-plots of zincian georgeite (such changes would be expected in the case of impurity phases such as $ZnCO_3$) (Extended Data Fig. 5).

X-ray pair distribution function (PDF) analysis, which does not suffer from phenomena related to scattering-path phasing, indicated that georgeite and zincian georgeite have strikingly similar and strong short-range order up to 5 Å (Fig. 3d); subtle differences appear between 5 Å and 10 Å, with georgeite exhibiting less long-range order. The extended order seen upon addition of zinc could be responsible for the enhanced stability of zincian georgeite prepared by co-precipitation[16]. A comparison of the georgeite PDF with a calculated PDF of malachite[22]

(Fig. 3e) shows that georgeite is not simply a nanoscale form of malachite (a phenomenon noted for other amorphous minerals, such as iron sulphide[23]): the complete absence of the 15.27 Å correlation between crystallographically identical copper atoms in georgeite shows that local ordering operates well below the length scales associated with the malachite unit cell. PDF matching to other copper phases such as aurichalcite[24], azurite[25] and rosasite[26] confirmed georgeite to be a material distinct from any known copper hydroxycarbonate (Extended Data Fig. 5).

After synthesis, the zincian georgeite and malachite precursors were calcined at 300 °C to form copper-oxide/zinc-oxide intermediates, and then reduced to the active catalyst phase. We find that the intermediate materials produced on calcination and the final-state catalysts both exhibit a microstructure that reflects the structural characteristics of their precursor phase. In the case of SAS-prepared zincian georgeite, calcination produced disordered copper oxide/zinc oxide with nanocrystals of 3–4 nm in diameter, as observed by STEM and PDF analysis (Extended Data Figs 6 and 7). The extent of the disorder resulted in XRD and XANES analysis showing no discernible metal-oxide contribution, although subtle changes in the EXAFS data were observed (Extended Data Fig. 8). Disordered copper-oxide species have previously been reported to have copper-edge XANES data that fit with a Jahn–Teller distorted octahedron[27], as with the calcined zincian georgeite. We found that the nanocrystallinity of the SAS-prepared zincian georgeite persisted until the residual high-temperature carbonate
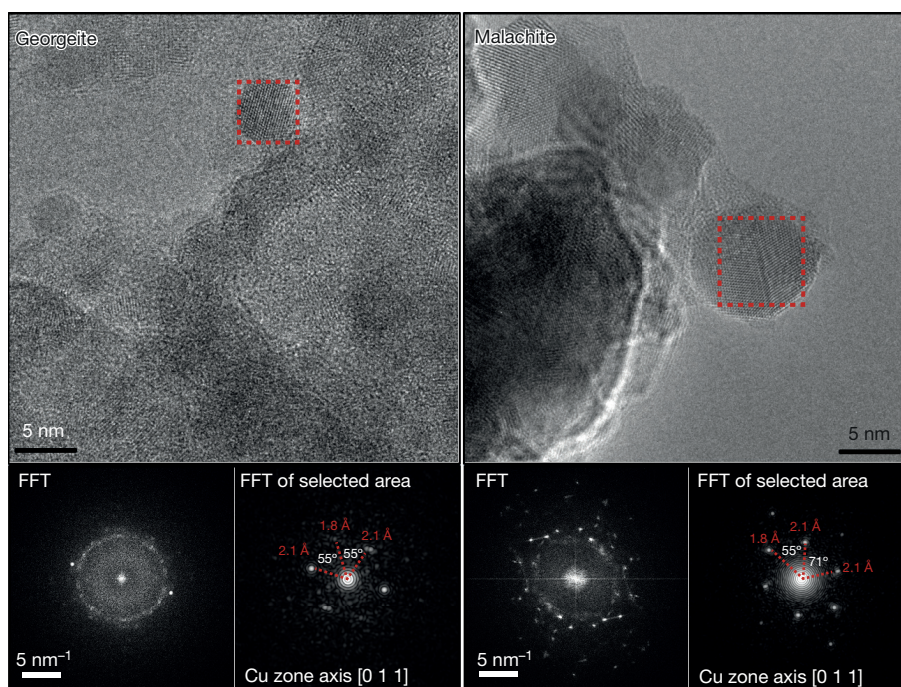
Figure 4 | Characterization, by environmental transmission electron microscopy, of the microstructure of the reduced final-state catalysts derived from zincian georgeite and zincian malachite. Calcined materials were reduced under a H_2 pressure of 2 mbar and a temperature of 225 °C. The representative images shown in the top panels reveal distinct Cu nanoparticles distributed on ZnO for both samples. This was confirmed by fast Fourier transform (FFT) analysis, shown in the bottom panels. The reduced malachite sample generally has larger Cu nanoparticles than the georgeite sample. Also, there is a substantially greater Cu–ZnO interaction in the georgeite-derived sample than in the malachite-derived catalyst. The georgeite sample has a complex mix of Cu and poorly defined ZnO particles (as revealed by diffuse rings in the large-scale FFTs); the malachite sample shows better-defined, phase-separated Cu and ZnO. The oxidation state of Cu was monitored by means of electron energy-loss spectroscopy, which revealed that Cu was in its metallic state in both samples under the reduction conditions (Extended Data Fig. 9f). The Cu zone axis is the direction (as determined by analysis of the FFT) along which the Cu crystallite is being observed.

decomposed to form XRD-discernible copper-oxide and zinc-oxide phases above 425 °C (Extended Data Fig. 7). Conversely, calcination of zincian malachite at temperatures greater than 300 °C produced crystalline, XRD- and XANES-observable, copper-oxide and zinc-oxide phases (Extended Data Fig. 7). A linear combination fit of the XANES data showed that 60% of the 300 °C calcined zincian malachite (Extended Data Fig. 8) was associated with copper oxide and zinc oxide, whereas these phases were not present in the calcined zincian georgeite. STEM showed that 300 °C calcined zincian malachite (Extended Data Fig. 6) was composed of copper-oxide and zinc-oxide grains with much longer-range crystalline order than the corresponding calcined zincian georgeite.

The nanocrystalline nature of calcined zincian georgeite translates to a high copper surface area ($53 \, m^2 \, g^{-1}$) and small mean copper crystallite size (7.4 ± 0.7 nm) when the material is reduced. Environmental transmission electron microscopy (ETEM) carried out under reducing conditions shows a complex mixture of copper particles and exceptionally small, disordered zinc-oxide grains (the mean zinc-oxide crystallite size was 2.8 ± 1.6 nm, as judged by XRD), with notable interactions between copper and zinc oxide (Fig. 4). By comparison, the more crystalline zincian-malachite-derived copper oxide/zinc oxide had a lower copper surface area ($35 \, m^2 \, g^{-1}$) and a microstructure composed of distinctly larger copper particles (mean crystallite size was 14.2 ± 3.8 nm, by XRD) and zinc oxide particles (mean crystallite size was 5.6 ± 3.6 nm by XRD). This difference in particle size and structural order is reflected in the smaller copper–copper and zinc–zinc coordination numbers noted for the zincian-georgeite-derived catalyst from *in situ* EXAFS analysis (Extended Data Fig. 9). On a macroscopic level, strong interactions between copper and zinc oxide, as shown by XPS observations of partial ZnO_x coverage of copper on reduction[8], were observed for both catalysts (Extended Data Fig. 9). However, ETEM shows considerably more interactions between copper and zinc oxide in the catalyst that was derived from disordered zincian georgeite.

Methanol-synthesis activity is well known to correlate strongly with copper surface area[28], and a large interfacial area between copper and zinc oxide has been reported to produce highly active methanol-synthesis catalysts[29], containing active sites that are associated with surface-defect copper sites decorated by zinc[8]. However, we find that 40 hours of LTS conditions markedly decrease the copper surface areas of catalysts derived from both zincian georgeite ($53 \pm 3 \, m^2 \, g^{-1}$ to $17 \pm 1 \, m^2 \, g^{-1}$) and zincian malachite ($38 \pm 2 \, m^2 \, g^{-1}$ to $19 \pm 1 \, m^2 \, g^{-1}$)— yet the catalysts were still active after this time period, clearly indicating that copper surface areas do not adequately correlate with catalyst activity in this reaction. We surmise that the high activity of our catalyst can be explained by a combination of a greater content of exposed copper, and an intimate interface contact between copper and zinc oxide, inherited from the zincian-georgeite precursor. Moreover, the SAS method produces very pure zincian georgeite with a low content of sodium ions, without requiring an aqueous washing step; this high purity might also contribute to both the high activity and the stability of the zincian-georgeite-derived LTS catalyst.

1. Bridge, P. J., Just, J. & Hey, M. H. Georgeite, a new amorphous copper carbonate from the Carr Boyd Mine, Western Australia. *Mineral. Mag.* **43,** 97–98 (1979).
2. Spencer, M. S. The role of zinc oxide in Cu/ZnO catalysts for methanol synthesis and the water-gas shift reaction. *Top. Catal.* **8,** 259–266 (1999).
3. Behrens, M. Meso- and nano-structuring of industrial Cu/ZnO/(Al$_2$O$_3$) catalysts. *J. Catal.* **267,** 24–29 (2009).
4. Fujitani, T. & Nakamura, J. The effect of ZnO in methanol synthesis catalysts on Cu dispersion and the specific activity. *Catal. Lett.* **56,** 119–124 (1998).

5. Chinchen, G. C., Denny, P. J., Jennings, J. R., Spencer, M. S. & Waugh, K. C. Synthesis of methanol. Part 1. Catalysts and kinetics. *Appl. Catal.* **36,** 1–65 (1988).
6. Rhodes, C., Hutchings, G. J. & Ward, A. M. Water-gas shift reaction: finding the mechanistic boundary. *Catal. Today* **23,** 43–58 (1995).
7. Short, G. D., Chinchen, G. C. & Williamson, J. G. Synthesis of methanol; finely divided oxides of zinc, aluminum, magnesium; with metallic copper. US patent 4,788,175 (1988).
8. Behrens, M. *et al.* The active site of methanol synthesis over Cu/ZnO/Al$_2$O$_3$ industrial catalysts. *Science* **336,** 893–897 (2012).
9. Baltes, C., Vukojevic, S. & Schueth, F. Correlations between synthesis, precursor, and catalyst structure and activity of a large set of CuO/ZnO/Al$_2$O$_3$ catalysts for methanol synthesis. *J. Catal.* **258,** 334–344 (2008).
10. Bems, B. *et al.* Relations between synthesis and microstructural properties of copper/zinc hydroxycarbonates. *Chemistry* **9,** 2039–2052 (2003).
11. Pollard, A. M. *et al.* Georgeite and azurite as precursors in the preparation of coprecipitated copper/zinc oxide catalysts. *Appl. Catal. A* **85,** 1–11 (1992).
12. Prieto, G., de Jong, K. P. & de Jongh, P. E. Towards 'greener' catalyst manufacture: reduction of wastewater from the preparation of Cu/ZnO/Al$_2$O$_3$ methanol synthesis catalysts. *Catal. Today* **215,** 142–151 (2013).
13. Tang, Z.-R. *et al.* New nanocrystalline Cu/MnO$_x$ catalysts prepared from supercritical antisolvent precipitation. *ChemCatChem* **1,** 247–251 (2009).
14. Reverchon, E. Supercritical antisolvent precipitation of micro- and nano-particles. *J. Supercrit. Fluids* **15,** 1–21 (1999).
15. Rogers, A. P. A review of the amorphous minerals. *J. Geol.* **25,** 515–541 (1917).
16. Pollard, A. M., Thomas, R. G., Williams, P. A., Just, J. & Bridge, P. J. The synthesis and composition of georgeite and its reactions to form other secondary copper(II) carbonates. *Mineral. Mag.* **55,** 163–166 (1991).
17. Behrens, M. *et al.* Performance improvement of nanocatalysts by promoter-induced defects in the support material: methanol synthesis over Cu/ZnO:Al. *J. Am. Chem. Soc.* **135,** 6061–6068 (2013).
18. Campbell, J. S. Influences of catalyst formulation and poisoning on the activity and die-off of low temperature shift catalysts. *Ind. Eng. Chem. Process Des. Dev.* **9,** 588–595 (1970).
19. Schur, M. *et al.* Continuous coprecipitation of catalysts in a micromixer: nanostructured Cu/ZnO composite for the synthesis of methanol. *Angew. Chem. Int. Edn* **42,** 3815–3817 (2003).
20. Rothe, J., Hormes, J., Bonnemann, H., Brijoux, W. & Siepen, K. In situ X-ray absorption spectroscopy investigation during the formation of colloidal copper. *J. Am. Chem. Soc.* **120,** 6019–6023 (1998).
21. Klokishner, S. *et al.* Cation ordering in natural and synthetic (Cu$_{1-x}$Zn$_x$)$_2$CO$_3$(OH)$_2$ and (Cu$_{1-x}$Zn$_x$)$_5$(CO$_3$)$_2$(OH)$_6$. *J. Phys. Chem. A* **115,** 9954–9968 (2011).
22. Behrens, M. & Girgsdies, F. Structural effects of Cu/Zn substitution in the malachite-rosasite System. *Z. Anorg. Allg. Chem.* **636,** 919–927 (2010).
23. Michel, F. M. *et al.* Short- to medium-range atomic order and crystallite size of the initial FeS precipitate from pair distribution function analysis. *Chem. Mater.* **17,** 6246–6255 (2005).
24. Harding, M. M., Kariuki, B. M., Cernik, R. & Cressey, G. The structure of aurichalcite, (CuZn)$_5$(OH)$_6$(CO$_3$)$_2$ determined from a microcrystal. *Acta Crystallogr. B* **50,** 673–676 (1994).
25. Belokoneva, E. L., Gubina, Y. K. & Forsyth, J. B. The charge density distribution and antiferromagnetic properties of azurite Cu$_3$[CO$_3$]$_2$(OH)$_2$. *Phys. Chem. Miner.* **28,** 498–507 (2001).
26. Perchiazzi, N. & Merlino, S. The malachite-rosasite group: crystal structures of glaukosphaerite and pokrovskite. *Eur. J. Mineral.* **18,** 787–792 (2006).
27. Belin, S. *et al.* CuAu/SiO$_2$ catalysts for the selective oxidation of propene to acrolein: the impact of catalyst preparation variables on material structure and catalytic performance. *Catal. Sci. Technol.* **3,** 2944–2957 (2013).
28. Chinchen, G. C., Waugh, K. C. & Whan, D. A. The activity and state of the copper surface in methanol synthesis catalysts. *Appl. Catal.* **25,** 101–107 (1986).
29. Behrens, M. *et al.* The potential of microstructural optimization in metal/oxide catalysts: higher intrinsic activity of copper by partial embedding of copper nanoparticles. *Chem. Cat. Chem.* **2,** 816–818 (2010).

METHODS

Material preparation. *SAS method for preparing georgeite and zincian georgeite.* Copper(II) acetate monohydrate (4 mg ml^{-1}) and zinc(II) acetate dihydrate (2.16 mg ml^{-1}) (Sigma Aldrich ≥ 99% Puriss) were dissolved in ethanol (reagent grade, Fischer Scientific) containing 0 vol%, 5 vol% or 10 vol% deionized water. Smithsonite ZnCO$_3$ was prepared with zinc(II) acetate dehydrate (2.16 mg ml^{-1}) in a 10 vol% water and ethanol solution. SAS experiments were performed using apparatus manufactured by Separex. CO$_2$ (from BOC) was pumped through the system (held at 110 bar, 40 °C) via the outer part of a coaxial nozzle at a rate of 6 kg h^{-1}. The metal salt solution was concurrently pumped through the inner nozzle, using an Agilent HPLC pump at a rate of 6.4 ml min^{-1}. The resulting precipitate was recovered on a stainless steel frit, while the CO$_2$–solvent mixture passed down stream, where the pressure was decreased to separate the solvent and CO$_2$. The precipitation vessel has an internal volume of 1 litre. Precipitation was carried out for 120 minutes, and followed by a purge of the system with ethanol–CO$_2$ for 15 minutes, then CO$_2$ for 60 minutes under 110 bar and 40 °C. The system was then depressurized and the dry powder collected. Recovered samples were placed in a vacuum oven at 40 °C for 4 hours to remove any residual solvent. Approximately 1.5 g of georgeite is prepared during the 120-minute duration of solution precipitation.

Co-precipitation method for preparing malachite and zincian malachite precursors for the standard methanol-synthesis catalysts. The procedure was performed via a semi-continuous process, using two peristaltic pumps to maintain pH. Copper(II) nitrate hydrate and zinc(II) nitrate hydrate solutions in deionized water were prepared with copper/zomc molar ratios of 1/0, 1/1 and 2/1. The premixed metal solution (5 l, ~0.5 g ml^{-1}) was preheated along with a separate 5 l solution of 1.5 M sodium carbonate. The mixed metals were precipitated by combining the two solutions concurrently at 65 °C, with the pH being held between 6.5 and 6.8. The precipitate would spill over from the small precipitation pot into a stirred ageing vessel, held at 65 °C. The precipitate was aged for 15 minutes after all precursor solutions had been used.

The precipitate was than filtered and washed to minimize sodium content. The sample was washed with 6 l of hot deionized water, and the sodium content monitored using a photometer. The washing process was repeated until the sodium content showed no change. The sample was then dried at 110 °C for 16 hours. Samples were calcined for 6 hours at 300 °C or 450 °C in a tube furnace under static air. The ramp rate used to reach the desired temperature was 1 °C min^{-1}.

Catalyst testing. Catalyst testing was performed with 0.5 g of the calcined catalyst, pelleted and ground to a sieve fraction of 0.6–1 mm for both the methanol-synthesis and the LTS test reactions. The catalysts were reduced *in situ* using a 2% H$_2$/N$_2$ gas mixture at 225 °C (ramp rate 1 °C min^{-1}), before the reaction gases were introduced. Data reported for the industrial standards are the mean value from four repeat experiments. Error bars are based on the standard deviation from the mean values.

Methanol synthesis. Testing was carried out in a single-stream, six-fixed-bed reactor with an additional bypass line. After reduction, the catalysts were then subjected to synthesized syngas (CO/CO$_2$/H$_2$/N$_2$ = 6.9/2/67/17.8) at 3.5 l h^{-1}, 25 bar pressure and 195 °C. In-line gas analysis was performed using an FT-IR spectrometer, which detected CO, CO$_2$, H$_2$O and CH$_3$OH. Downstream of the catalyst beds, knockout pots collected effluent produced from the reaction. The contents were collected after each test run and analysed using gas chromatography to evaluate the selectivity of catalysts. The total system flow was maintained using the bypass line.

LTS. Testing was performed in six parallel fixed-bed reactors with a single stream feed and an additional bypass line. After reduction, the catalysts were subjected to synthetic syngas (CO/CO$_2$/H$_2$/N$_2$ = 1/4/13.75/6.25) at 27.5 bar pressure and 220 °C. The reactant gas stream was passed though vaporized water to give a water composition of 50 vol%. This gives a total gas flow of H$_2$O/CO/CO$_2$/H$_2$/N$_2$ = 50/2/8/27.5/12.5. The standard mass hourly space velocity (MHSV) used for testing was 75,000 k h^{-1} kg^{-1}. In-line IR analysis was carried out to measure CO conversion. Selectivity was determined by the methanol content within the knockout pots downstream of the reactors. Space and mass velocity variation tests were performed at 65 hours' time-on-line by altering the flow for each catalyst bed. Relative activities were calculated by altering the flow for each catalyst bed in order to achieve 75% CO conversion after 75 hours' time-on-line. The total system flow was maintained using the bypass line.

Characterization methods. *Powder X-ray diffraction (XRD).* Measurements were performed using a PANalytical X'pert Pro diffractometer with a Ni-filtered CuK$_α$ radiation source operating at 40 kV and 40 mA. Patterns were recorded over the range of 10–80° 2θ using a step size of 0.016°. All patterns were matched using the International Centre for Diffraction Data (ICDD) database. An *in situ* Anton Parr XRK900 cell (with an internal volume of ~0.5 l) was used to monitor the formation of metallic copper during the reduction of the CuO/ZnO materials. A flow of 2% H$_2$/N$_2$ (60 ml min^{-1}) was passed through the sample bed while the cell was heated to 225 °C (ambient temperature to 125 °C, ramp rate 10 °C min^{-1}; 125–225 °C, ramp

rate 2 °C min^{-1}). The sample was then cooled to room temperature and a 20–100° 2θ scan performed. Copper crystallite size was estimated from a peak-broadening analysis of the XRD pattern using Topas Academic[30], and the volume-weighted column height (L_{vol}) was calculated according to ref. 31.

X-ray absorption fine-edge spectroscopy (XAFS). K-edge XAFS studies of copper and zinc were carried out on the B18 beamline at the Diamond Light Source, Didcot, UK. Measurements were performed using a quick extended (QE) XAFS set-up with a fast-scanning silicon (111) double-crystal monochromator. The time resolution of the spectra reported herein was 1 minute per spectrum ($k_{max} = 14$), and on average three scans were acquired to improve the signal-to-noise ratio of the data. All *ex situ* samples were diluted with cellulose and pressed into pellets to optimize the effective-edge step of the XAFS data and measured in transmission mode using ion-chamber detectors. All transmission XAFS spectra were acquired concurrently with the appropriate reference foil (copper or zinc) placed between I_t and I_{ref} XAS data processing, and EXAFS analysis were performed using IFEFFIT[32] with the Horae package[33] (Athena and Artemis). The FT data were phase-corrected for oxygen. The amplitude-reduction factor, s_0^2, was derived from EXAFS data analysis of a known copper reference compound, namely tenorite (CuO). For the fitting of the local coordination geometry of georgeite and malachite, the Jahn–Teller distorted copper–oxygen bond was difficult to observe because of thermal disorder, and so was fixed in the model.

X-ray pair distribution function (PDF) analysis. Synchrotron X-ray PDF data were collected on the 11-ID-B beamline at the Advanced Photon Source, Argonne National Laboratory, and on the I15 beamline at the Diamond Light Source. Powder samples were packed into kapton capillaries with an internal diameter of 1 mm. Room-temperature powder X-ray diffraction data were collected at a wavelength of 0.2114 Å (11-ID-B) and 0.1620 Å (I15) using the Rapid Acquisition PDF method[34]. The scattering data ($0.5 \leq Q \leq 22$ Å^{-1}) were processed into PDF data using the program GudrunX[35]. Two notations of PDF data are presented in this manuscript: $G(r)$ and $D(r)$ (ref. 36). The total radial distribution function, $G(r)$, is the probability of finding a pair of atoms, weighted by the scattering power of the pair, at a given distance, r; it is the Fourier transform experimentally determined total structure factor. $D(r)$ is re-weighted to emphasize features at high r, such that $D(r) = 4\pi r \rho_0 G(r)$, where ρ_0 is the average number density of the material (in atoms Å^{-1}).

Fourier transform-infrared spectroscopy (FT-IR). Analysis was carried out using a Jasco FT/IR 660 Plus spectrometer in transmission mode over a range of 400–4,000 cm^{-1}. Catalysts were supported in a pressed KBr disk.

Raman spectroscopy. Raman spectra were obtained using a Renishaw inVia spectrometer equipped with an argon ion laser ($\lambda = 514$ nm).

Thermal gravimetric analysis (TGA). TGA measurements were performed using a SETARAM Labsys analyser with sample masses of about 20 mg, at 1 °C min^{-1} under air with a flow rate of 20 ml min^{-1}.

Evolved gas analysis (EGA). EGA experiments were performed using a Hiden CATLAB under the same conditions used in the TGA experiments.

Copper surface area analysis. This was determined by reactive frontal chromatography. Catalysts were crushed and sieved to a particle size of 0.6–1 mm and packed into a reactor tube. The catalyst was purged under helium for 2 minutes at 70 °C before being heated under a 5% H$_2$ reduction gas to 230 °C (8 °C min^{-1}) for 3 hours. The catalyst was then cooled to 68 °C under helium before the dilute 2.5% N$_2$O reaction gas was added with a flow rate of 65 ml min^{-1}. The formation of N$_2$ from the surface oxidation of the copper catalyst by N$_2$O was measured downstream using a thermal conductivity detector (TCD). Once the surface of the copper is fully oxidized, there is a breakthrough of N$_2$O, detected on the TCD. From this, the number of oxygen atoms that are chemisorbed on the copper surface can be determined. The number of exposed surface copper atoms and the copper surface area can then be derived. Quoted surface areas are calculated using discharged sample mass. Note that recent work[37,38] has shown that, if the catalyst is exposed to partial pressures of H$_2$ exceeding 0.05 bar, then partial reduction of ZnO at the copper interface can occur. This will affect copper surface area results, owing to N$_2$O oxidizing both copper and ZnO$_x$. In these cases, alternative techniques, such as a H$_2$ thermal conductivity detector, will give more accurate data with respect to copper surface area[37,38].

Copper surface area analysis after exposure to LTS conditions. Copper surface area analysis of the fresh catalysts were carried out on a Quantachrome ChemBET 3000. Sample (100 mg) was packed into a stainless-steel U-tube and purged with high-purity helium for 5 minutes. Samples were reduced using 10% H$_2$/Ar (30 ml min^{-1}) heated to 140 °C at 10 °C min^{-1}, before heating further to 225 °C at 1 °C min^{-1}. The resulting catalyst was held at this temperature for 20 minutes to ensure that complete reduction took place. Note that, under this partial pressure of H$_2$, it has been reported that ZnO species in contact with copper can partially reduce[37,38]. Residual H$_2$ was flushed from the system by switching the gas line back over to helium (80 ml min^{-1}), while holding the sample at 220 °C for another 10 minutes.

The temperature was then reduced to 65 °C for N_2O pulsing (BOC AA Grade). A programme of 12 pulses of 113 μl N_2O with a 5-minute stabilization time between pulses was carried out, followed by three pulses of N_2 for calibration. Unreacted N_2O was trapped before reaching the detector using a molecular sieve 5A (pelleted, 1.6 mm, Sigma Aldrich) trap. The copper surface area was determined from the amount of N_2 emitted and the post-reaction analysis of catalyst mass, as follows:

Copper surface area $(m^2 g^{-1})$ = N_2 volume (ml) $\times N_A \times 2$/Catalyst mass (g) $\times 24{,}000$ (ml) $\times (1.47 \, 10^{19})$ $(atoms \, m^{-2})$

where N_A is the Avogadro constant, 6.022×10^{23} (atoms). The key assumptions are that the amount of N_2 emitted amounts to half a monolayer's coverage of oxygen, and that the surface density of copper is 1.47×10^{19} (atoms m^{-2}). The volume of N_2 produced was quantified using a TCD.

After copper surface area analysis, the samples were kept under N_2 and transferred to an LTS reactor. Ageing was carried out in a single fixed-bed reactor equipped with a bypass line. CO, N_2, CO_2 and H_2 were introduced to the catalyst bed via mass-flow controllers (Bronkhorst). Water of high-performance liquid chromatography (HPLC) grade was passed through a liquid-flow controller (Bronkhorst) and then into a controlled evaporator mixer (Bronkhorst) that was heated to 140 °C. N_2 was fed through the vaporized water to give a dilute syngas mixture ($H_2O/CO/CO_2/H_2/N_2 = 25/1/4/13.75/56.25$). This mixture was introduced at 220 °C after re-reduction of the catalyst. The gas flows were controlled to achieve an MHSV of $30{,}000 \, l \, h^{-1} \, kg^{-1}$. After ageing for 40 hours, the samples were transferred back to the Quantachrome ChemBET Chemisorption analyser, whereby, after re-reduction, the copper surface areas of the aged catalysts were measured, as described above.

Scanning transmission electron microscopy (STEM). Samples for STEM characterization were dry-dispersed onto holey carbon TEM grids. They were examined in an aberration-corrected JEOL ARM-200CF scanning transmission electron microscope operating at 200 kV in bright-field and dark-field STEM imaging modes. Reliable electron microscopy results could be obtained only from the set of zincian-georgeite- and zincian-malachite-derived materials, as these were found to be stable under the vacuum environment of the microscope, and largely unaffected by electron-beam irradiation. By way of contrast, the copper-only georgeite precursor materials were highly unstable under vacuum conditions (even without electron-beam irradiation), turning from a blue to dark-green colour, probably owing to the loss of occluded water. The corresponding zincian-georgeite materials showed no such colour transformation under vacuum.

Environmental transmission electron microscopy (ETEM). Samples for reduction during characterization by ETEM were dry-dispersed on heater chips (DensSolution trough hole) and then mounted on a DensSolution SH30 heating holder. The holder with sample was inserted into an FEI Titan 80-300 environmental transmission electron microscope operated at 300 kV (ref. 39) . The reduction of the samples was performed *in situ* as follows, for both the georgeite and the malachite precursors: a flow of H_2 was let into the microscope, building up a pressure of 2 mbar. The sample was heated from room temperature to 150 °C using a heating ramp rate of 10 °C min^{-1}. The final heating to 225 °C was done at 1 °C min^{-1}. The oxidation state of copper was monitored by electron energy-loss spectroscopy (EELS) during the reduction treatment using a Gatan Tridiem 866 spectrometer attached to the microscope. After an extended *in situ* treatment of several hours at 225 °C, phase-contrast lattice imaging was performed at elevated

temperature in an H_2 atmosphere for both the georgeite and malachite samples, and recorded using a Gatan US 1000 charge-coupled-device camera.

X-ray photoelectron spectroscopy (XPS). A Kratos Axis Ultra DLD system was used to collect XPS spectra, using a monochromatic Al K_α X-ray source operating at 120 W. Data were collected with pass energies of 160 eV for survey spectra, and 40 eV for the high-resolution scans. The system was operated in the Hybrid mode, using a combination of magnetic immersion and electrostatic lenses and acquired over an area approximately $300 \times 700 \, \mu m^2$. A magnetically confined charge-compensation system was used to minimize charging of the sample surface, and the resulting spectra were calibrated to the C(1 s) line at 284.8 eV; all spectra were taken with a 90° take-off angle. A base pressure of $\sim 1 \times 10^{-9}$ Torr was maintained during collection of the spectra. Gas treatments were performed in a Kratos catalysis cell, which mimics the conditions of a normal reactor vessel, allowing the re-creation of reactor conditions and analysis of the chemical changes taking place on the catalyst surface. Briefly, the cell consists of a fused quartz reactor vessel contained within a stainless-steel vacuum chamber (base pressure $\sim 10^{-8}$ Torr after baking). Samples were heated at a controlled ramp rate of 2 °C min^{-1} to a temperature of 225 °C using a eurotherm controller. The catalysts were exposed to an atmosphere of 2% H_2 in nitrogen with a flow rate of 30 ml min^{-1}, controlled using MKS mass flow controllers during the heating ramp, during the 20-minute isotherm at 225 °C, and also while the catalyst was cooled to 25 °C. The samples were analysed before and after gas treatment without breaking the vacuum.

Inductively coupled plasma mass spectrometry (ICP-MS) and carbon–hydrogen–nitrogen (CHN) analysis. These analyses were provided as a commercial service by Warwick Analytical Services.

Helium pycnometry. This analysis was provided as a commercial service by MCA Services.

30. Coelho, A. A. TOPAS Academic: General Profile and Structure Analysis Software for Powder Diffraction Data (Bruker AXS, Karlsruhe, 2010).
31. Balzar, D. *et al.* Size-strain line-broadening analysis of the ceria round-robin sample. *J. Appl. Cryst.* **37,** 911–924 (2004).
32. Newville, M. IFEFFIT: interactive XAFS analysis and FEFF fitting. *J. Synchrotron Radiat.* **8,** 322–324 (2001).
33. Ravel, B. & Newville, M. ATHENA, ARTEMIS, HEPHAESTUS: data analysis for X-ray absorption spectroscopy using IFEFFIT. *J. Synchrotron Radiat.* **12,** 537–541 (2005).
34. Chupas, P. J. *et al.* Rapid-acquisition pair distribution function (RA-PDF) analysis. *J. Appl. Cryst.* **36,** 1342–1347 (2003).
35. Soper, A. K. & Barney, E. R. Extracting the pair distribution function from white-beam X-ray total scattering data. *J. Appl. Cryst.* **44,** 714–726 (2011).
36. Keen, D. A. A comparison of various commonly used correlation functions for describing total scattering. *Angew. Chem. Int. Edn* **53,** 7043–7047 (2014).
37. Fichtl, M. B. *et al.* Counting of oxygen defects versus metal surface sites in methanol synthesis catalysts by different probe molecules. *J. Appl. Cryst.* **34,** 172–177 (2001).
38. Kuld, S., Conradsen, C., Moses, P. G., Chorkendorff, I. & Sehested, J. Quantification of zinc atoms in a surface alloy on copper in an industrial-type methanol synthesis catalyst. *Angew. Chem. Int. Edn* **53,** 5941–5945 (2014).
39. Hansen, T. W., Wagner, J. B. & Dunin-Borkowski, R. E. Aberration corrected and monochromated environmental transmission electron microscopy: challenges and prospects for materials science. *Mater. Sci. Technol.* **26,** 1338–1344 (2010).
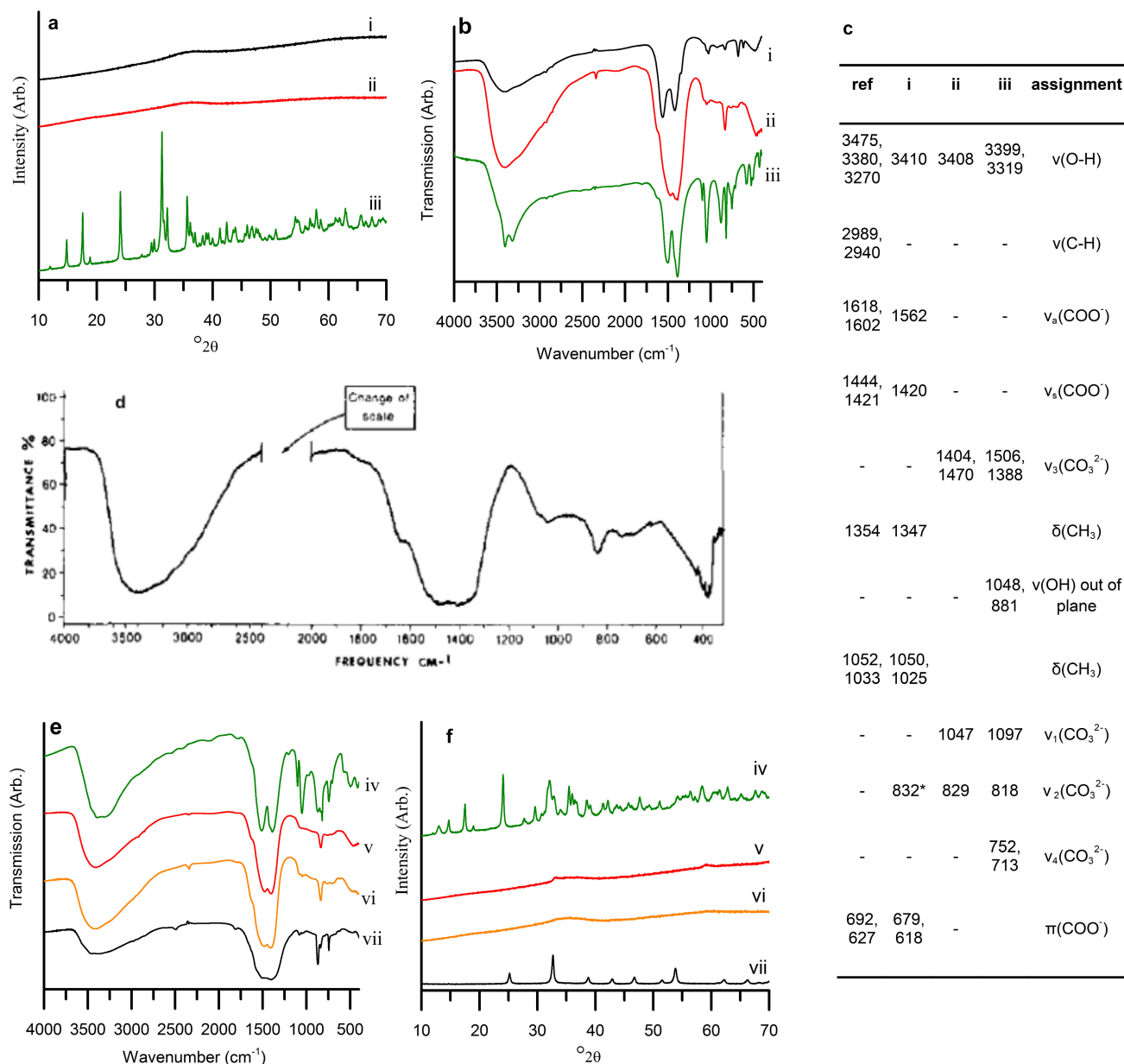
Extended Data Figure 1 | FT-IR and XRD characterization of SAS copper and copper/zinc acetate precipitates. Key: i, SAS-prepared copper acetate; ii, SAS-prepared georgeite; iii, malachite prepared by co-precipitation; iv, 2/1 copper/zinc malachite prepared by co-precipitation; v, SAS-prepared 2/1 copper/zinc georgeite; vi, SAS-prepared 1/1 copper/zinc georgeite; vii, SAS-prepared zmithsonite ($ZnCO_3$). **a**, XRD analysis of copper-only samples. **b**, FT-IR analysis of copper-only samples. **c**, FT-IR band assignment of copper-only samples, with (reference) designated as received copper(II) acetate monohydrate. Values given are for IR band positions in wavenumbers (cm^{-1}). *The presence of this band shows that SAS precipitation with no additional water co-solvent produced some georgeite as well as amorphous copper acetate. We attribute the formation of georgeite to the small amount of water present from the monohydrated starting salt. **d**, IR spectrum of mineralogical georgeite, reproduced with the permission of the Mineralogical Society of Great Britain and Ireland from ref. 11. **e**, FT-IR spectra of copper/zinc samples. **f**, XRD of copper/zinc samples.

a

Sample	Elemental composition					Density	Na content
	Cu (wt.%)	Zn (wt.%)	C (wt.%)	H (wt.%)	Calculated formula	g cm^{-3}	$\mu g_{Na} g^{-1}$
SAS copper (II) acetate	46.6	-	12.9	2.3	-	2.50	-
SAS georgeite	50.4	-	6.8	1.5	$Cu_{7.1}(CO_3)_5(OH)_{4.1}.4.6H_2O$ $Cu_7(CO_3)_5(OH)_4.5H_2O$	3.06	-
Mineralogical georgeite[a]	47.3	-	5.3	2.4	$Cu_5(CO_3)_3(OH)_4.6H_2O$	2.6*	-
Georgeite synthesised from sulphates[b]	57.8	-	5.5	0.9	$Cu_2CO_3(OH)_2$	2.4-2.8*	-
2:1 Cu:Zn SAS zincian georgeite	34.3	17.5	5.6	1.2	$(Cu_{0.66}Zn_{0.34})_{5.2}(CO_3)_3(OH)_{4.3}.3.4H_2O$ $(Cu_{0.66}Zn_{0.34})_5(CO_3)_3(OH)_4.3H_2O$	3.03	66
1:1 Cu:Zn SAS zincian georgeite	24.1	27.8	6.7	1.3	$Cu_{7.1}(CO_3)_5(OH)_{4.3}.3.5H_2O$ $Cu_7(CO_3)_5(OH)_4.4H_2O$	-	-
Co-precipitated malachite	55.4	-	5.4	1.0	$(Cu)_{1.9}(CO_3)(OH)_{1.9}0.3H_2O$ $(Cu)_2(CO_3)(OH)_2$	3.91	-
Co-precipitated (2:1 Cu:Zn malachite)	38.4	17.8	5.0	0.9	$(Cu_{1.5}Zn_{0.7})(CO_3)(OH)_{2.2}$ $(Cu_{0.66}Zn_{0.34})_2(CO_3)(OH)_2$	3.85	498

b

Sample	Calculated mass loss* (%)	Experimentally observed mass loss	Calculated/ Experimental (%)
SAS georgeite	38	37	103
SAS zincian georgeite	32	35	91
malachite	30	31	97
Zincian malachite	28	30	93

c
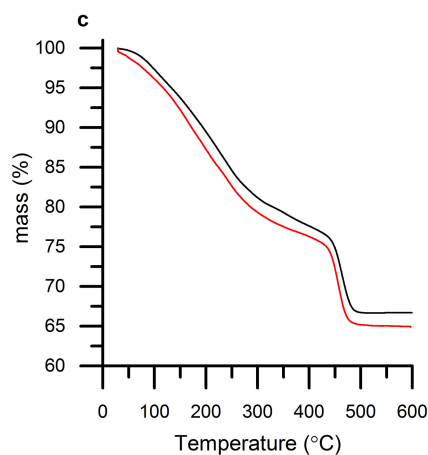
Extended Data Figure 2 | Elemental composition of copper and copper/zinc samples, with supplementary TGA analysis. a, Elemental composition of SAS-prepared georgeite and co-precipitated malachite samples. Elemental composition was determined by CHN analysis and ICP-MS. Densities were determined by helium pycnometry. [a]Values from ref. 11. [b]Values from ref. 16. *Density determined by sink–float (SF) method. The helium pycnometry used in our present study provides a skeletal density that negates buoyancy effects. **b**, Comparison of experimental and calculated mass losses for georgeite and malachite from TGA measurements. *Calculated from the assumption of final products being 2/1 copper oxide/zinc oxide. The lower-than-expected mass losses for the zincian phases could be associated with the inclusion of copper ions in the zinc oxide lattice. **c**, TGA analysis of 2/1 copper/zinc georgeite (red line) and 1/1 copper/zinc georgeite (black line).
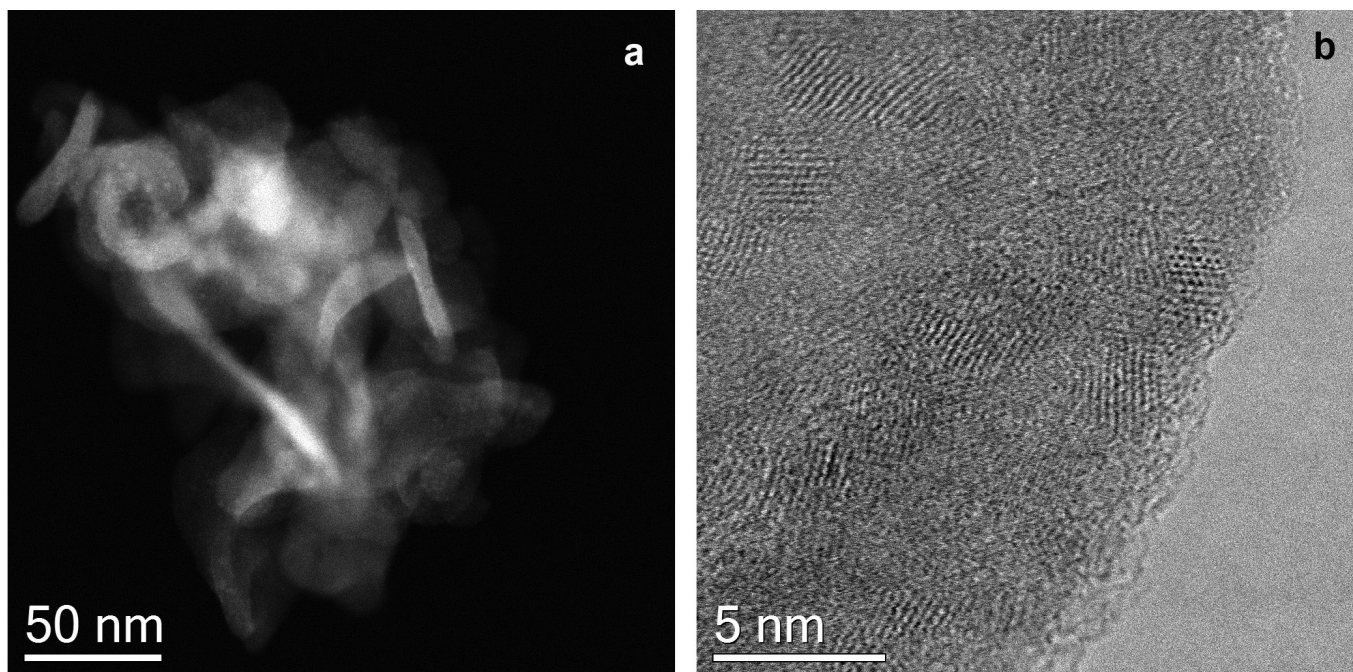
Extended Data Figure 3 | Representative STEM micrographs of the zincian georgeite precursor. Left, dark-field (DF) STEM micrograph. Right, bright-field (BF) micrograph. The general morphology of the zincian-georgeite precursor is shown in the DF-STEM micrograph. It typically consists of very characteristic, irregularly shaped agglomerates, about 100–200 nm in diameter, that are composed of 'amorphous' non-faceted particles about 40 nm wide. Closer inspection by BF-STEM shows that these non-faceted particles consist of an amorphous matrix phase in which are embedded largely disconnected, sub-2-nm crystallites of ordered material exhibiting clear lattice fringes. The amorphous matrix, probably containing the carbonate and hydroxyl species, is by far the majority phase, while the nanocrystallites make up less than 10% of the material by volume. This observation is consistent with our other characterization data, as signals from the matrix phase would dominate the XAFS analysis, whereas the nanocrystallites are too small in dimension to be detected by XRD. Analysis of fringe spacings and interplanar angles of individual nanocrystallites from such images suggests that some of the grains could be CuO (tenorite, where the copper is fourfold coordinated by oxygen), while others fit better to Cu_2O (cuprite, where the copper has a coordination number of 2). No convincing matches of the lattice fringes to either ZnO or $ZnCO_3$ could be found.

g
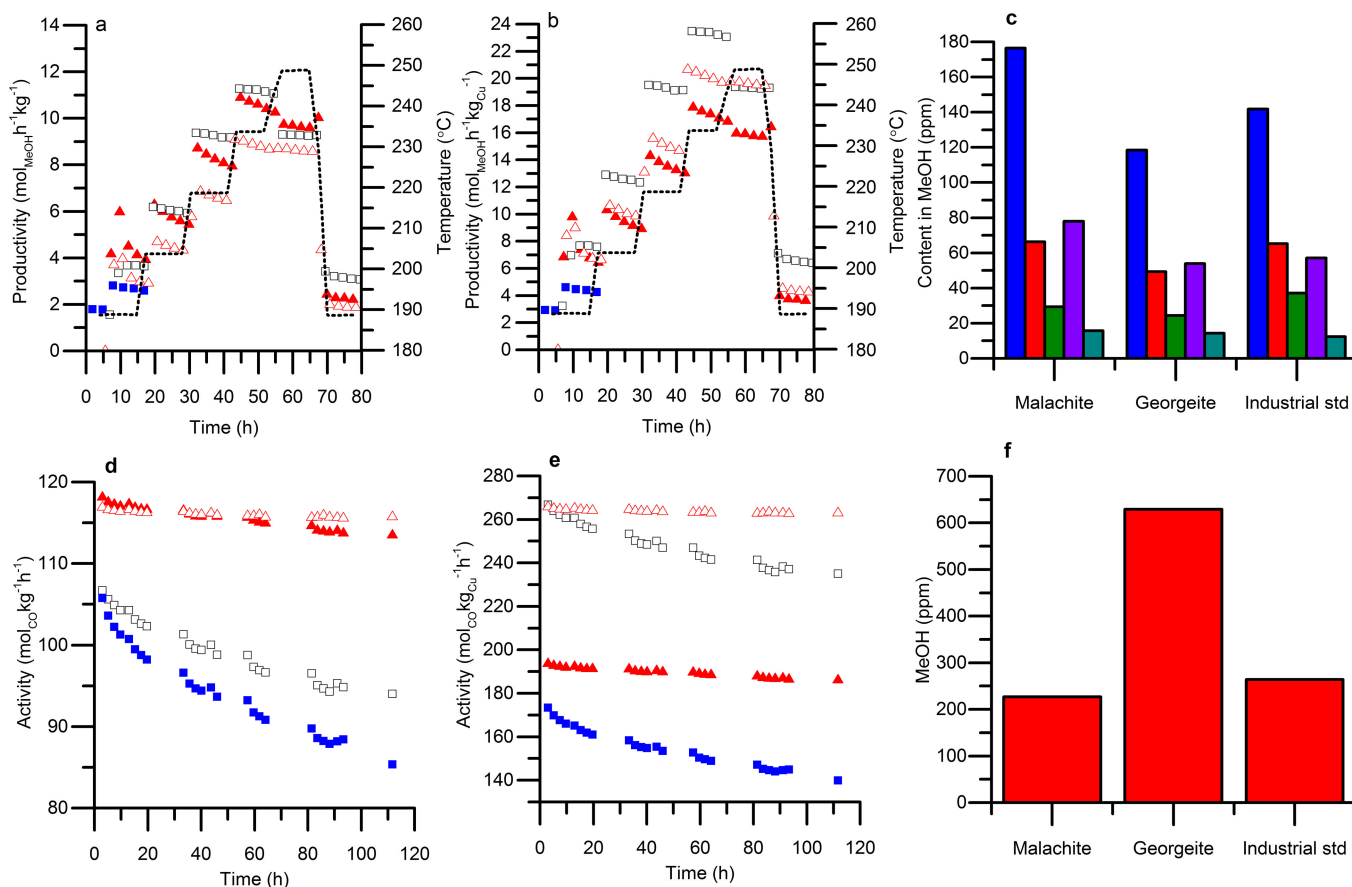
|	Methanol synthesis productivities normalised by copper surface area* ($mol_{methanol}$ m^{-2} h^{-1})§		LTS activities normalised by copper surface area (10^3 mol_{CO} m^{-2} h^{-1})*^	
	Initial productivity	Steady state	Initial productivity	Steady state
2:1 Cu:Zn Zincian georgeite derived	112.6	73.9	1.62	n/a
1:1 Cu:Zn Zincian georgeite derived	77.5	57.0	1.72	n/a
2:1 Cu:Zn Zincian malachite derived	80.2	74.1	2.21	n/a
Industrial catalysts	90.7	89.7	1.76	n/a

Extended Data Figure 4 | Further catalyst testing in methanol-synthesis and LTS reactions. Filled red triangles, 2/1 Cu/Zn georgeite; open triangles, 1/1 Cu/Zn georgeite; open squares, industrial standard; filled blue squares, 2/1 Cu/Zn malachite (this test was terminated after 190 °C because of poor activity). **a**, **b**, Methanol-synthesis data, normalized to total catalyst mass (**a**) and copper mass (**b**), at 190–250 °C. The dashed line shows the representative reactor-bed temperature. Reaction conditions were as follows: pressure 25 bar; gas composition $CO/CO_2/H_2/N_2 = 6/9.2/67/17.8$; MHSV = 7,200 l kg^{-1} h^{-1}. **c**, Concentration of byproducts that were collected in the condensate pot after the methanol-synthesis reaction, as determined by gas-chromatographic (GC) analysis. Byproducts are: ethanol (blue), propanol (red), butanol (green), iso-butanol (purple), and methyl iso-butyl ketone (turquoise). **d**, **e**, LTS-reaction data, normalized to total catalyst mass (**d**) and copper mass (**e**). Reaction conditions were as follows: temperature 220 °C; pressure

27.5 bar; gas composition $H_2O/CO/CO_2/H_2/N_2 = 50/2/8/27.35/12.5$; MHSV = 75,000 l kg^{-1} h^{-1}. **f**, Concentration of methanol collected in the condensate pot after the LTS reaction, as determined by GC analysis. **g**, Methanol-synthesis productivities and LTS activities, normalized by copper surface area. *Copper surface area analysis determined by N_2O reactive frontal chromatography before testing. §Methanol-synthesis data acquired at 190 °C, with steady state being at 18 hours' time-on-line. ^LTS data acquired at 220 °C, with steady state being at 40 hours time-on-line. Note that LTS simulation testing showed that copper surface area dropped markedly after 40 hours (to 17 m^2 g^{-1} and 19 m^2 g^{-1} for zincian-georgeite-derived and zincian-malachite-derived catalysts, respectively). The inverse correlation between copper surface area and initial productivity also suggests that loss of surface area occurs rapidly during the reaction and that the initial rate data are therefore likely to be inaccurate.
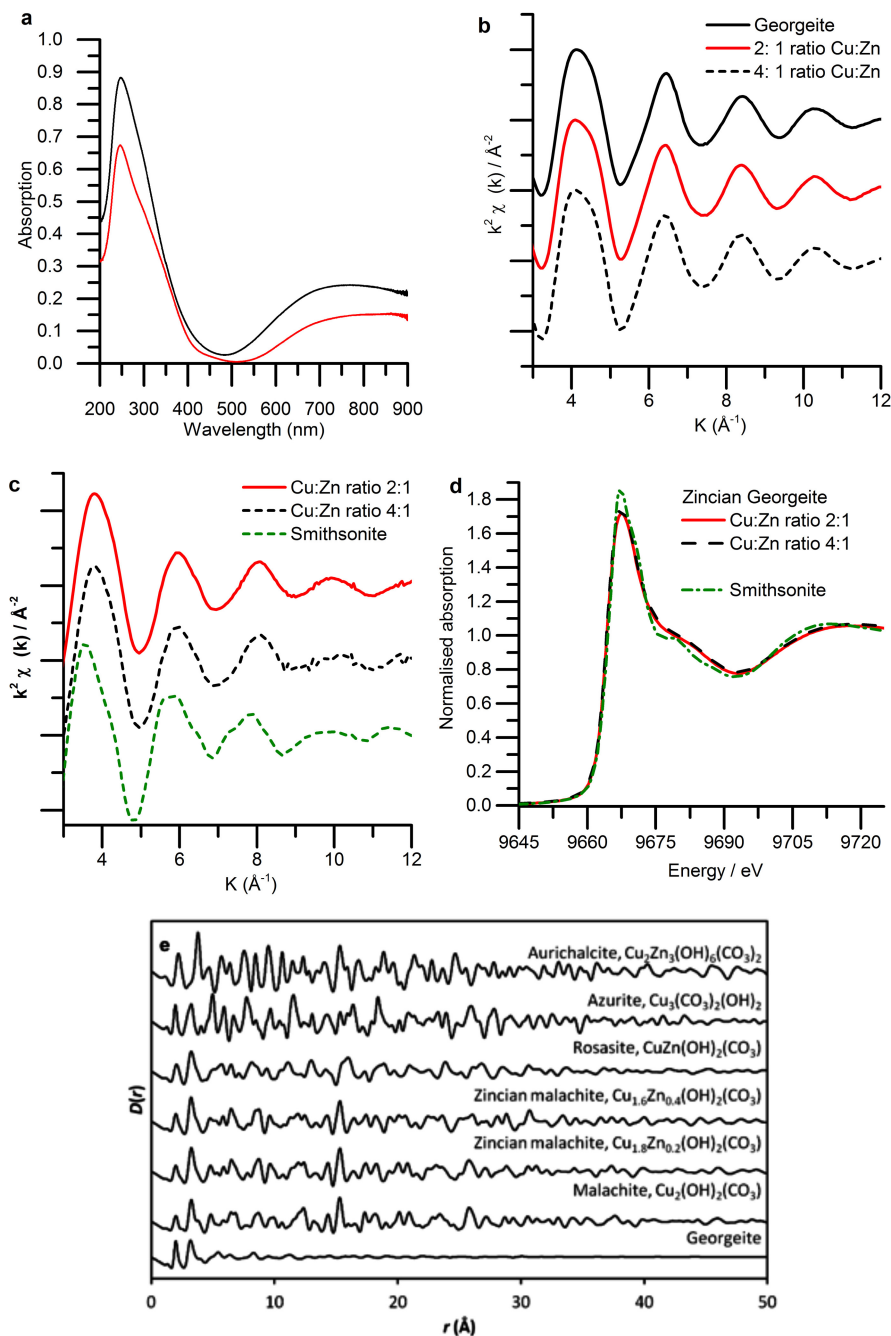
Extended Data Figure 5 | Spectroscopic analysis of the addition of zinc to georgeite. a, Diffuse reflectance UV–vis spectra of zincian malachite (red) and zincian georgeite (black). **b**, Copper K-edge EXAFS (χ) comparison of zincian georgeite (with a 4/1 or 2/1 copper/zinc ratio) with georgeite. **c**, Zinc K-edge XANES comparison of zincian georgeite with SAS-prepared smithsonite. **d**, Zinc K-edge EXAFS (χ) comparison of zincian georgeite with SAS-prepared smithsonite. **e**, Comparison of observed georgeite PDF data with simulated data for crystalline hydroxycarbonate minerals with similar compositions to that of georgeite—namely aurichalcite, azurite, rosasite, zincian malachite and malachite.
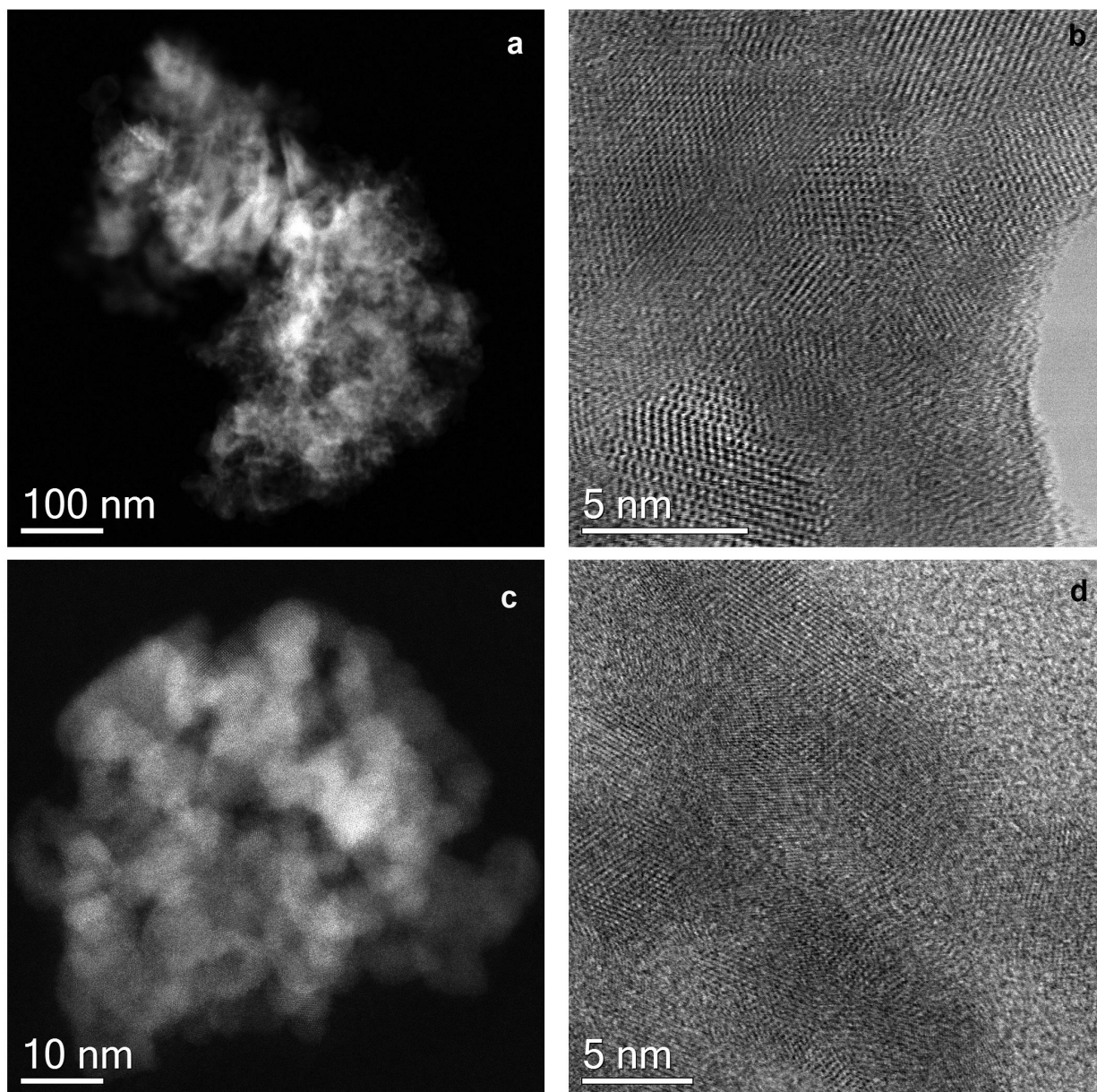
Extended Data Figure 6 | Representative DF-STEM and BF-STEM micrographs of zincian georgeite and zincian malachite, calcined at 300 °C. a, DF-STEM of calcined zincian georgeite. Higher-magnification imaging reveals that, after much of the carbonate and hydroxyl content is lost by calcination, most of the disordered matrix material in the precursor has crystallized, and only a small amount of amorphous material remains. The crystallized material is entirely in a nanocrystalline form, with a mean grain diameter of 3–4 nm, which is just below the detection limit for XRD. Analysis of the fringe spacings and interplanar angles from individual grains suggests that the material is now mainly an intimate mixture of zinc and copper oxides; the small amount of disordered material corresponds to the residual occluded carbonate material, as detected by TGA/EGA analysis of this material. **b**, BF-STEM of calcined zincian georgeite. **c**, DF-STEM of calcined zincian malachite. **d**, BF-STEM of calcined zincian malachite.
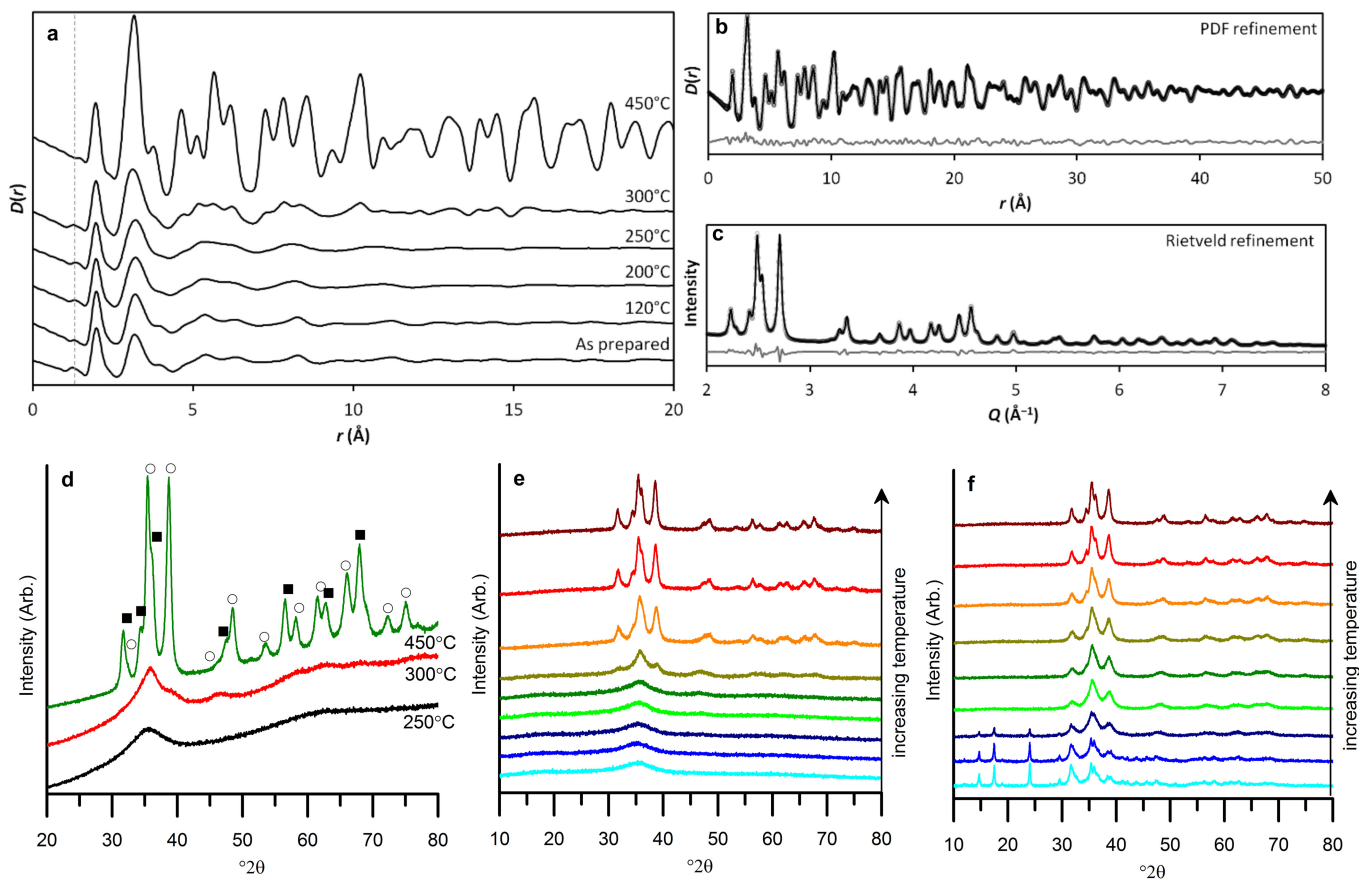
Extended Data Figure 7 | X-ray diffraction analysis of calcined zincian georgeite and zincian malachite. a, PDF of zincian georgeite, as prepared and after calcination at 120 °C, 200 °C, 250 °C, 300 °C and 450 °C. There is little change in the observed PDF up to 250 °C, other than a slight peak broadening, which can be attributed to a reduction in short-range order. The dashed line shows the position of the C–O peak, which is retained until temperatures higher than 300 °C. **b**, PDF and **c**, Rietveld fits of zincian georgeite after calcination at 450 °C. The measured data are shown as open circles; the fit is a solid black line; the difference is a grey line. Both techniques determine the product to be a mixture of copper oxide and zinc oxide (weight ratio of 68/32 by PDF; 67.7(4)/32.3(4) by Rietveld). **d**, *Ex situ* XRD patterns following calcination of zincian georgeite for 2 hours at 250 °C, 300 °C and 450 °C. Open circles, copper oxide; filled squares, zinc oxide. **e**, **f**, *In situ* XRD analysis of zincian georgeite (**d**) and zincian malachite (**e**) during calcination between 300 °C and 500 °C under an atmosphere of static air, with XRD scans every 25 °C.
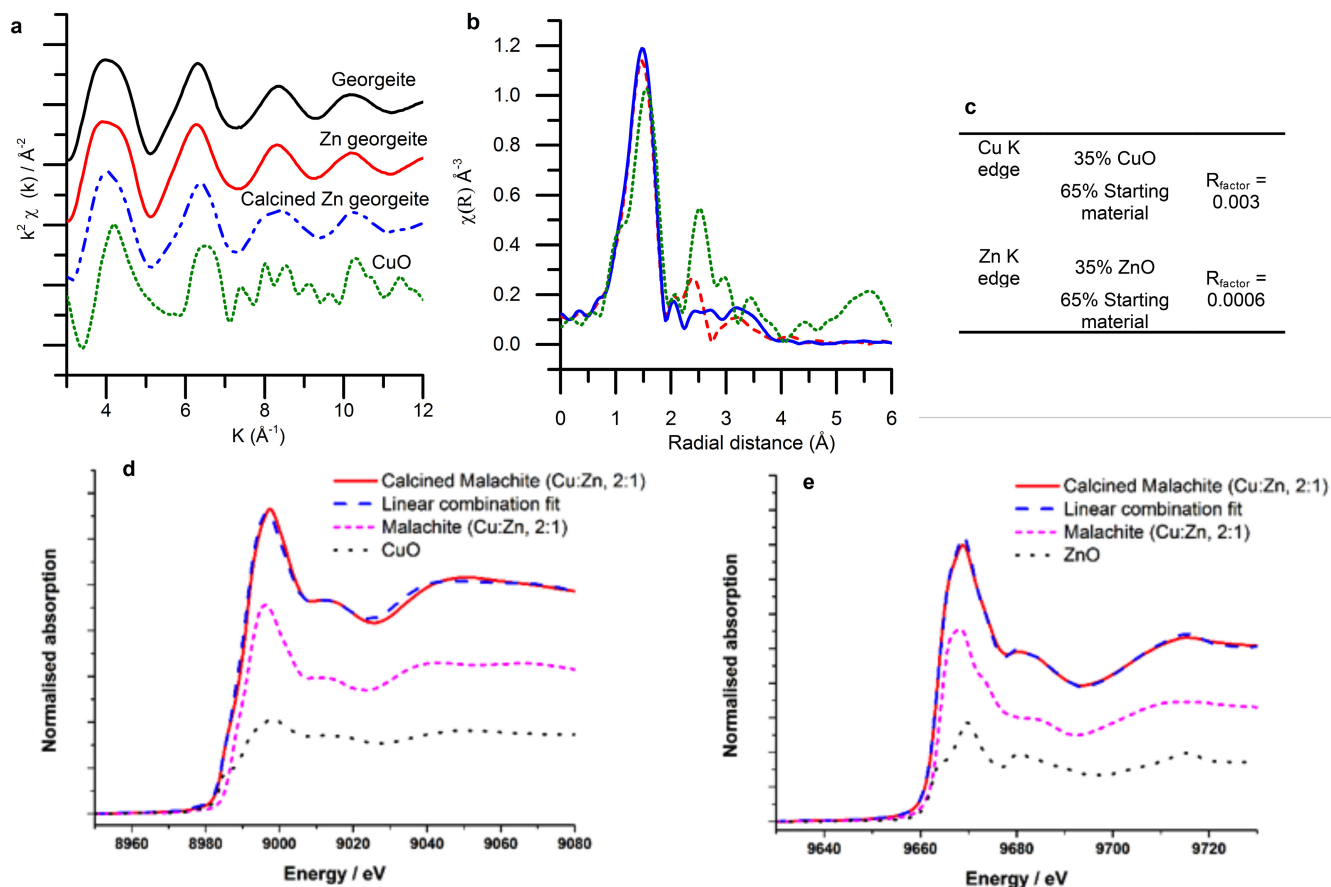
Extended Data Figure 8 | Copper K-edge XAFS analysis of zincian georgeite and zincian malachite calcined at 300 °C. a, EXAFS (χ) comparison of copper oxide, calcined zincian georgeite, zincian georgeite and georgeite. **b**, EXAFS (R) comparison of copper oxide (green), calcined zincian georgeite (black) and zincian georgeite (blue). **c–e**, Linear combination fit of copper oxide and zinc oxide with zincian malachite calcined at 300 °C.
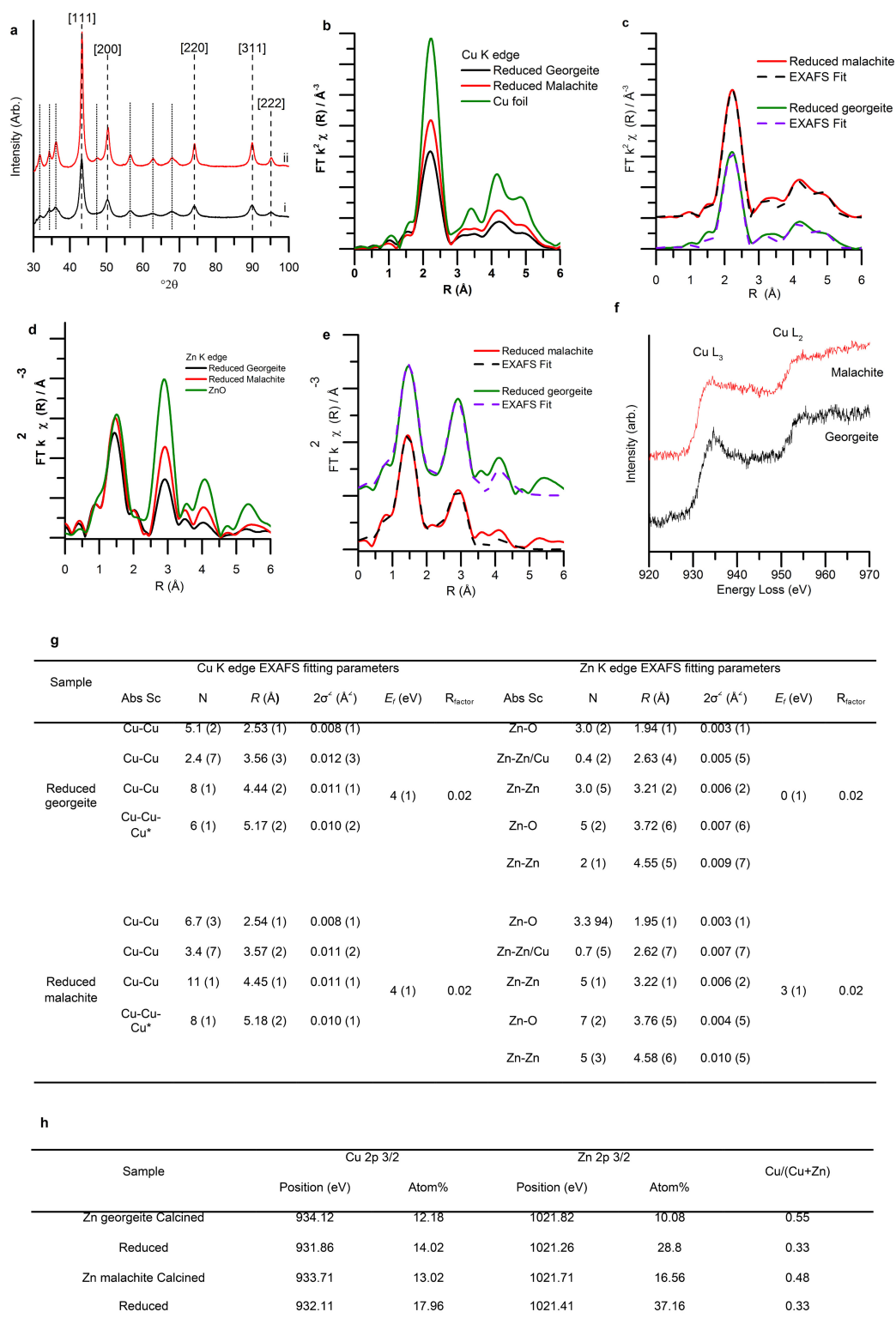
Extended Data Figure 9 | *In situ* characterization of final-state, reduced copper/zinc-oxide catalysts derived from zincian georgeite and zincian malachite, calcined at 300 °C. a, XRD of zincian-georgeite-derived catalyst after *in situ* hydrogen reduction (2% H_2/N_2 at 225 °C for 1 hour). Fine dotted lines indicate zinc-oxide reflections; dashed lines indicate metallic copper. **b**, Copper K-edge EXAFS Fourier transorm of final reduced catalysts derived from zincian georgeite and zincian malachite. **c**, Copper K-edge EXAFS fit of reduced catalysts. **d**, Zinc K-edge EXAFS Fourier transform of final reduced catalysts derived from zincian georgeite and zincian malachite. **e**, Zinc K-edge EXAFS fit of reduced catalysts. **f**, Electron energy-loss spectra (EELS) of georgeite and malachite, respectively, during reduction in the ETEM experiment. The EELS data

were acquired in 2 mbar H_2 at 225 °C, and show the fine structure of the Cu $L_{2,3}$ ionization edges, which are characteristic of metallic Cu^0. **g**, EXAFS fitting data for copper and zinc K-edge data. Fitting parameters for K-edge copper: amplitude-reduction factor $(S_0^2) = 0.91$, as deduced from copper-foil standard; fit range $3 < k < 11.2$, $1 < R < 5.5$ (with *k* denoting the fitting window from the χ data, and *R*, the path length, denoting the fitting from the Fourier transform of the χ data); number of independent points = 23; *denotes multiple scattering path. Fitting parameters for K-edge Zn: $s_0^2 = 0.90$ as deduced from a ZnO_2 standard; fit range $3.3 < k < 9.5$, $1 < R < 4.8$; number of independent points = 16; *denotes multiple scattering path. **h**, XPS analysis of calcined and reduced catalysts derived from zincian georgeite and zincian malachite.

g

Sample	Cu K edge EXAFS fitting parameters						Zn K edge EXAFS fitting parameters					
	Abs Sc	N	*R* (Å)	2σ² (Å²)	E_f (eV)	R_{factor}	Abs Sc	N	*R* (Å)	2σ² (Å²)	E_f (eV)	R_{factor}
Reduced georgeite	Cu-Cu	5.1 (2)	2.53 (1)	0.008 (1)			Zn-O	3.0 (2)	1.94 (1)	0.003 (1)		
	Cu-Cu	2.4 (7)	3.56 (3)	0.012 (3)			Zn-Zn/Cu	0.4 (2)	2.63 (4)	0.005 (5)		
	Cu-Cu	8 (1)	4.44 (2)	0.011 (1)	4 (1)	0.02	Zn-Zn	3.0 (5)	3.21 (2)	0.006 (2)	0 (1)	0.02
	Cu-Cu-Cu*	6 (1)	5.17 (2)	0.010 (2)			Zn-O	5 (2)	3.72 (6)	0.007 (6)		
							Zn-Zn	2 (1)	4.55 (5)	0.009 (7)		
Reduced malachite	Cu-Cu	6.7 (3)	2.54 (1)	0.008 (1)			Zn-O	3.3 94	1.95 (1)	0.003 (1)		
	Cu-Cu	3.4 (7)	3.57 (2)	0.011 (2)			Zn-Zn/Cu	0.7 (5)	2.62 (7)	0.007 (7)		
	Cu-Cu	11 (1)	4.45 (1)	0.011 (1)	4 (1)	0.02	Zn-Zn	5 (1)	3.22 (1)	0.006 (2)	3 (1)	0.02
	Cu-Cu-Cu*	8 (1)	5.18 (2)	0.010 (1)			Zn-O	7 (2)	3.76 (5)	0.004 (5)		
							Zn-Zn	5 (3)	4.58 (6)	0.010 (5)		

h

Sample	Cu 2p 3/2		Zn 2p 3/2		Cu/(Cu+Zn)
	Position (eV)	Atom%	Position (eV)	Atom%	
Zn georgeite Calcined	934.12	12.18	1021.82	10.08	0.55
Reduced	931.86	14.02	1021.26	28.8	0.33
Zn malachite Calcined	933.71	13.02	1021.71	16.56	0.48
Reduced	932.11	17.96	1021.41	37.16	0.33

Extended Data Table 1 | EXAFS fitting parameters for georgeite and malachite

Abs Sc	N	R (Å)	$2\sigma^2$ (Å^2)	E_f (eV)	R_{factor}
Malachite					
Cu–O	4 (fixed)	1.92 (2)	0.007 (2)		
Cu–O	2 (fixed)	2.45 (7)	0.02 (1)		
Cu–C	3 (fixed)	3.01 (4)	0.002 (6)	-1(1)	0.014
Cu–Cu	2 (fixed)	3.12 (4)	0.006 (5)		
Cu–Cu	3 (fixed)	3.31 (3)	0.007 (3)		
Georgeite					
Cu–O	4 (fixed)	1.94 (1)	0.004 (1)	2(1)	0.007
Cu–O	2 (fixed)	2.45 (fixed)	0.03 (fixed)		

Fitting parameters for malachite: $S_0^2 = 0.72$ as deduced from a copper-oxide standard; fit range $3 < k < 12$, $1 < R < 3.5$; number of independent points $= 14$. Fitting parameters for georgeite: $s_0^2 = 0.72$ as deduced from a copper-oxide standard; fit range $3 < k < 12$, $1 < R < 3.5$; number of independent points $= 14$. Abs Sc; scattering path, N; coordination number (first shell); R, path length, σ^2: Debye–Waller factor, E_f; change in edge energy, R_{factor}; goodness of fit.